






RESEARCH ARTICLE | AUGUST 09 2024

Role of Atwood number in the shock-induced evolution of a double-layer gas cylinder

Xin Li (李昕) ; Jiaao Hao (郝佳傲)  ; Chih-Yung Wen (温志湧) ; E. Fan (范镔) 



Physics of Fluids 36, 082105 (2024)

<https://doi.org/10.1063/5.0221371>



Articles You May Be Interested In

Effects of Mach and Atwood numbers on the shock-induced evolution of a double-layer gas cylinder

Physics of Fluids (February 2024)

A study on dynamics of shock-accelerated forward-facing triangular bubbles at different Atwood numbers

Physics of Fluids (January 2024)

Numerical simulation of the interaction between a planar shock wave and a backward-facing triangular bubble containing gases with different Atwood numbers

Physics of Fluids (April 2024)



Physics of Fluids

Special Topics Open
for Submissions

[Learn More](#)

Role of Atwood number in the shock-induced evolution of a double-layer gas cylinder

Cite as: Phys. Fluids **36**, 082105 (2024); doi: [10.1063/5.0221371](https://doi.org/10.1063/5.0221371)

Submitted: 31 May 2024 · Accepted: 24 July 2024 ·

Published Online: 9 August 2024



View Online



Export Citation



CrossMark

Xin Li (李忻),¹ Jiaao Hao (郝佳傲),^{1,a)} Chih-Yung Wen (温志湧),¹ and E. Fan (范鐸)²

AFFILIATIONS

¹Department of Aeronautical and Aviation Engineering, The Hong Kong Polytechnic University, Hung Hom, Kowloon, Hong Kong

²Department of Mechanics and Aerospace Engineering, Southern University of Science and Technology, Shenzhen 518055, China

^{a)} Author to whom correspondence should be addressed: jiaao.hao@polyu.edu.hk

ABSTRACT

An A/B/C-type gas cylinder with various concentrations of SF₆ (ranging from 5% to 80% in volume fraction) in the inner cylinder is constructed to investigate the dependence of the interface evolution on the Atwood number. For negative Atwood numbers, secondary vortex pairs emerge at the downstream interface of the outer cylinder following the interaction of a high-pressure triple point with the downstream interface, while a downstream jet is formed due to the generation of a notably higher-pressure zone after the transmitted shock wave traverses the convergence point. The widths and heights of both outer and inner cylinders are analyzed to quantify the interface evolution. The mechanism behind the vorticity evolution is investigated using the vorticity transport equation. The vorticity equation is introduced to investigate the mechanism of vorticity evolution. The dilatation and baroclinic terms play a dominant role in the dynamics of vorticity production. The net circulation can be predicted by linearly summing existing circulation models. Analysis of the area and mean mass fraction histories of the outer and inner cylinders shows that more ambient gas dilutes SF₆ and promotes gas mixing as the Atwood number decreases.

Published under an exclusive license by AIP Publishing. <https://doi.org/10.1063/5.0221371>

I. INTRODUCTION

The Richtmyer–Meshkov (RM) instability occurs at an interface between two fluids of different densities when subjected to a sudden acceleration.^{1,2} The perturbation at this interface leads to complex fluid motions and turbulent mixing. Moreover, RM instability widely exists in various scientific and engineering fields, including inertial confinement fusion (ICF),³ supernova explosions,⁴ and supersonic combustion engines.⁵

The interaction between shock waves and gas cylinders is of significance in the study of RM instability. Corresponding experimental and numerical investigations have been conducted to enhance our comprehension of RM instability. For the scenarios of the interaction between shock waves and single-layer gas cylinders, the evolution of shock-induced heavy- and light-gas cylinders was investigated through both experimental observations and numerical simulations.^{6–11} Ding *et al.* expanded the two-dimensional (2D) gas cylinder to a three-dimensional (3D) one and introduced a 3D theoretical model to forecast the upstream interface movements of both heavy- and light-gas cylinders.^{12,13} Moreover, the initial conditions including nonlinear acoustic effects and incoming shock intensities have a substantial influence on the morphologies of the gas cylinder, turbulent mixing, and jet formation.^{14–19} Bagabir and Drikakis¹⁴ numerically examined the

influences of Mach numbers on the interaction between the shock waves and cylindrical bubbles. Their findings indicated that bubble deformations occur and the velocity of the jet increases with the growth of Mach numbers. Niederhaus *et al.*¹⁵ investigated how different Atwood numbers and Mach numbers affect the interaction between shock waves and bubbles. They illustrated the significance of nonlinear acoustic effects and the generation of primary and secondary vorticity, especially for $M > 2$ and $A > 2$. The discussion regarding the types of jets and the mechanisms behind jet formation is extensively explored due to the influence of shock intensities and acoustic impedance.^{16–19}

However, RM instability is generally associated with multi-layer interface evolution. For example, there are usually several layers made of different materials in an ICF capsule, with the outer layer referred to as the ablator layer and the inner layer as the fuel layer.²⁰ In addition, fuel-atomized droplets contain air cavities in supersonic combustion engines. Therefore, it is crucial to research the issue of the multi-layer interface evolution in engineering applications. Previous studies primarily focused on the RM instability of an A/B/A-type fluid layer and an A/B/A-type gas cylinder, where two interfaces separate two kinds of gases (gas A and gas B). For an A/B/A-type fluid layer, Mikaelian^{21–24} developed a theoretical linear solution for the amplitude growth rates.

Henry de Frahan *et al.*²⁵ and Liu *et al.*²⁶ employed different analysis approaches to investigate the dependence of the perturbation growth on the initial conditions, such as the amplitude, phase difference, and Atwood numbers. Liang *et al.*^{27–29} and Cong *et al.*³⁰ proposed linear and nonlinear models to predict the growth of interface perturbations on both the heavy-fluid-layer and light-fluid-layer, considering additional instabilities at the two interfaces caused by reverberating waves within the fluid layer. Based on these studies, Cong *et al.*³⁰ studied the RM instability subjected to reshock, concentrating on the influence of initial layer thickness on interface growth and constructing a nonlinear model. For an A/B/A-type gas cylinder, Wang *et al.*³¹ illustrated the morphologies of gas rings and proposed a circulation prediction approach by linearly summing the results from circulation models. Feng *et al.*^{32,33} and Li *et al.*³⁴ studied the dependence of fluid evolution and turbulent mixing on the initial conditions, such as radius ratio, eccentricity, incident shock intensities, and Atwood numbers.

Compared to detailed studies on the A/B/A-type fluid layer, the A/B/C-type gas layer widely exists in engineering applications, where two interfaces separate three kinds of gases (gases A, B, and C). For instance, there is a CH form shell (35 mg ml^{-1}) existing between the outer shell (2.7 g ml^{-1}) and the inner shell (200 mg ml^{-1}) in a double-shell ICF capsule.^{35,36} The materials of different shells are completely dissimilar. Liang and Luo³⁷ focused on a gas layer with a light/medium/heavy density configuration. They introduced a linear model to assess amplitude growth and extended a nonlinear model to depict perturbation growth at the two interfaces. However, the ICF capsule exhibits a multi-layer spherical configuration, which differs from the gas layer. To simplify the analysis, the three-dimensional multi-layer spherical structure of the target capsule is approximated as a two-dimensional multi-layer cylinder. While numerous parameter studies have explored the interaction between planar shock waves and A/B/A-type gas cylinders, research on the interaction between shock waves and A/B/C-type gas cylinders remains lacking.

To fill this gap, this work uses a numerical approach for multi-component compressible flow to explore the flow morphologies of a double-layer gas cylinder with various concentrations of SF_6 in the inner cylinder. The formation of the secondary vortex pairs and downstream jets is discussed, and the mechanism of vorticity production is investigated. The net circulation of a double-layer gas cylinder is predicted by linearly summing circulation models. The impacts of the Atwood number on the gas mixing are explored by analyzing the area and mean mass fraction.

II. NUMERICAL METHODOLOGIES

A. Governing equations and numerical schemes

The 2D Navier–Stokes equations are employed to solve multi-component compressible flow. When chemical reactions are neglected, the governing equations for n_s species are given as follows:

$$\frac{\partial \mathbf{U}}{\partial t} + \frac{\partial (\mathbf{F} - \mathbf{F}_v)}{\partial x} + \frac{\partial (\mathbf{G} - \mathbf{G}_v)}{\partial y} = 0. \quad (1)$$

The conservative variable vector \mathbf{U} and inviscid fluxes \mathbf{F} and \mathbf{G} are defined as follows:

$$\mathbf{U} = \begin{bmatrix} \rho_1 \\ \vdots \\ \rho_{n_s} \\ \rho u \\ \rho v \\ E \end{bmatrix}, \quad \mathbf{F} = \begin{bmatrix} \rho_1 u \\ \vdots \\ \rho_{n_s} u \\ \rho u^2 + p \\ \rho uv \\ (E + p)u \end{bmatrix}, \quad \mathbf{G} = \begin{bmatrix} \rho_1 v \\ \vdots \\ \rho_{n_s} v \\ \rho uv \\ \rho v^2 + p \\ (E + p)v \end{bmatrix}, \quad (2)$$

where $\rho_i (i = 1 - n_s)$ and ρ signify the density of each species and the total density of the mixture, respectively; u and v represent the velocity components in the x and y directions, respectively; E is the total energy per unit volume; p denotes the pressure.

The expressions of the viscous fluxes \mathbf{F}_v and \mathbf{G}_v are given as follows:

$$\mathbf{F}_v = \begin{bmatrix} -J_{1,x} \\ \vdots \\ -J_{n_s,x} \\ \tau_{xx} \\ \tau_{xy} \\ u\tau_{xx} + v\tau_{xy} - q_x - \sum_{i=1}^{n_s} J_{i,x} h_i \end{bmatrix}, \quad (3)$$

$$\mathbf{G}_v = \begin{bmatrix} -J_{1,y} \\ \vdots \\ -J_{n_s,y} \\ \tau_{xy} \\ \tau_{yy} \\ u\tau_{xy} + v\tau_{yy} - q_y - \sum_{i=1}^{n_s} J_{i,y} h_i \end{bmatrix}, \quad (4)$$

where q_x and q_y refer to the heat conduction terms; $J_{i,x}$ and $J_{i,y}$ stand for the species diffusion terms; τ_{ij} represents the components of viscous stress; h_i denotes the enthalpy of each species.

In this work, an in-house multi-block parallel finite-volume CFD code called PHAROS^{38–40} is conducted to simulate the evolution of the double-layer gas cylinder. When solving the Riemann problems, the Godunov-type methods have been applied to estimate the inviscid fluxes due to their robustness and usefulness in computing flows with complex shock structures. The original Harten–Lax–van Leer (HLL) solver simplifies the Riemann problem to a shock and expansion wave pair, with a single average state in between. Despite its simplicity, this approach is notably dissipative. The Harten–Lax–van Leer Contact (HLLC) solver⁴¹ is an extension of the HLL scheme, which reduces the dissipation by restoring a contact discontinuity to the theoretical wave structure. The Godunov-type method is inherently free of spurious oscillations around shock waves but is restricted to first-order accuracy. To address this limitation, the monotone upstream-centered scheme for conservation law (MUSCL) reconstruction is extended to the Godunov-type method, achieving second-order accuracy in smooth parts of the flow while not interfering with the region of any discontinuity. The van Leer limiter, which provides the best accuracy reliably, is used in the MUSCL reconstruction.⁴² Viscous fluxes are

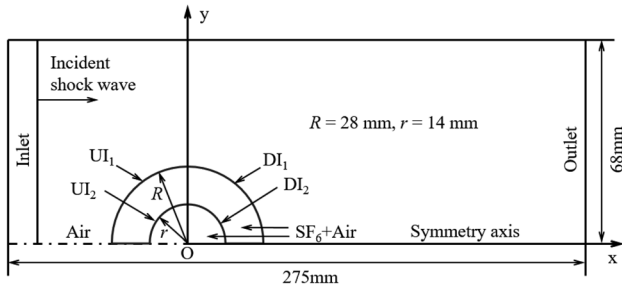


FIG. 1. Schematic of the computational domain.

calculated using a second-order central scheme. Temporal integration is conducted by using a three-step third-order Runge–Kutta method.

B. Computational settings and mesh convergence study

As shown in Fig. 1, the computational domain is a two-dimensional rectangle with a length of 275 mm and a width of 68 mm. To improve computational efficiency, the domain is set to half of the test section. The boundary conditions on the left and right boundaries are specified as inlet and outlet, while the lower and upper boundaries are set as symmetry and slip wall conditions. The center of the bubble is defined as the coordinate origin (0, 0). The radii of the outer and inner cylinders are 28 and 14 mm, respectively. The poles are defined as the intersection points of the symmetry axis with the interfaces of the double-layer gas cylinder. The incident shock (IS) propagates downstream from the left boundary. The moment when it reaches the upstream pole of the outer cylinder is denoted as $t = 0$, where t represents the physical time. The Mach number of IS is 1.27, the initial temperature $T_0 = 293$ K, and the initial pressure $p_0 = 101\,325$ Pa. The ambient gas is set as air, and the gases in the gas ring and inner cylinder are a mixture of air and SF_6 . For the baseline, the volume fraction of SF_6 in the gas ring and inner cylinder are 0.5 and 0.05, which are consistent with the experimental conditions in Table I. Physical properties regarding air and SF_6 are illustrated in Table II.

Grid independence is verified using uniform meshes with various sizes of 0.1, 0.2, and 0.4 mm, which are labeled meshes I–III. By comparing the density distribution along the symmetry axis at $t = 120\,\mu\text{s}$, it can be observed that there is a convergence in the curve of density distribution as the mesh resolution increases in Fig. 2. The Richardson extrapolation is introduced to quantitatively analyze the grid convergence. Starting with the series solution of the discretization error,

$$f = f_{\text{exact}} + g_1 h + g_2 h^2 + O(h^3), \quad (5)$$

where f denotes the grid solution, h is the grid spacing, g_1 and g_2 are functions independent of the grid spacing, and f_{exact} is the continuum

TABLE II. Physical properties of different gases at the initial condition.

Gas	Density (kg m^{-3})	Specific heat ratio	Sound speed (m s^{-1})	Acoustic impedance ($\text{kg m}^{-2} \text{s}^{-1}$)	Molecular weight (g mol^{-1})
Air	1.20	1.4	343	412	28.965
SF_6	6.14	1.1	136	835	146.055

TABLE I. Physical settings in the numerical simulation. M refers to the incident shock Mach number; R and r refer to the radii of the outer and inner cylinders, respectively; VF_1 and VF_2 refer to the volume fraction of SF_6 in the gas ring and the inner cylinder, respectively.

M	R (mm)	r (mm)	VF_1	VF_2	T_0 (K)	p_0 (Pa)
1.27	28	14	0.5	0.05	293	101 325

value at zero grid spacing. Equation (5) can be generalized for a p th order methods and r -value of mesh ratio as

$$f_{\text{exact}} \cong f_1 + \frac{f_1 - f_2}{r^p - 1}, \quad (6)$$

where p can be obtained from three solutions using the grid refinement ratio r ,

$$p = \ln \left(\frac{f_3 - f_2}{f_2 - f_1} \right) / \ln(r). \quad (7)$$

The Grid Convergence Index (GCI) measures the percentage difference between the computed value and the asymptotic numerical value. The GCI on the fine mesh is written as

$$GCI = \frac{F_s |\varepsilon|}{(r^p - 1)}, \quad (8)$$

where F_s is a factor of safety and set to 1.25, and ε is the relative error of quantity f . It is crucial that the solutions at each grid level must be in the asymptotic range of convergence, which can be checked by

$$GCI_{2,3} = r^p GCI_{1,2}, \quad (9)$$

Table III shows the grid spacing and the density at the intersection point of the symmetry axis and the UI_1 at $120\,\mu\text{s}$. The value of p is 5.158. The GCI for meshes I and II and meshes II and III are 0.016% and 0.588%, respectively. The calculated ratio of $GCI_{2,3}$ and $r^p GCI_{1,2}$ is 1.004, which is well within the asymptotic range of convergence. Based on the above-mentioned results, mesh I can be adopted to adequately resolve the flow.

In this study, the ambient gas is defined as air, and the gas in the gas ring is a mixture comprising 50% air and 50% SF_6 in volume fraction. To construct an A/B/C-type gas cylinder, the concentrations of SF_6 (ranging from 5% to 80% in volume fraction) are adjusted in the inner cylinder to investigate the dependence of the interface evolution on the Atwood number.

Here, the Atwood number quantifies the density ratio between the gas inside the bubble and its surrounding ambient gas, which is given by

$$A = \frac{\rho_2 - \rho_1}{\rho_2 + \rho_1}, \quad (10)$$

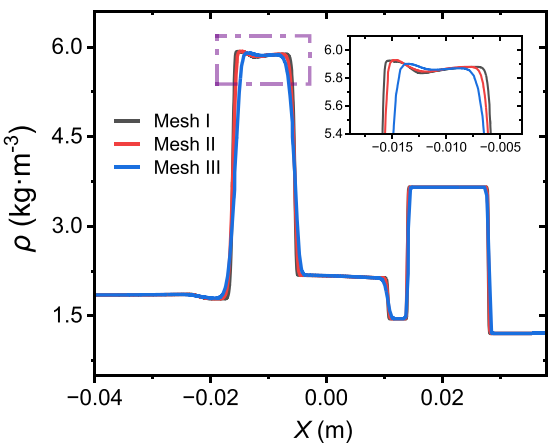


FIG. 2. Density distributions along the symmetry axis of the double-layer gas cylinder with different mesh sizes.

TABLE III. Mesh spacing and density at the intersection point of the symmetry axis and the UI_1 at $120\text{ }\mu\text{s}$ among different meshes. The calculated values of GCI between two meshes.

	Mesh spacing (mm)	Density (kg m^{-3})	GCI (%)
Mesh I	1	3.743	0.016
Mesh II	2	3.726	0.588
Mesh III	4	3.118	...

where ρ_1 and ρ_2 denote the densities of the ambient gas and the gas inside the gas ring for the outer layer, while ρ_1 and ρ_2 represent the densities of the gas inside the gas ring and inner cylinder for the inner layer in the scenario of the double-layer gas cylinder. Table IV lists the physical properties of the mixture at various layers along with their corresponding Atwood numbers. With an increase in the concentrations of SF_6 in the inner cylinder, both the densities of the mixed gases and their Atwood numbers rise, while the specific heat ratios decrease. When VF_2 approaches VF_1 , the absolute value of the Atwood numbers gets smaller.

TABLE IV. Physical properties of different gases at different layers.

Case		I	II	III	IV	V
Ambient gas (air)	Density (kg m^{-3})			1.20		
	Specific heat ratio			1.4		
Outer cylinder (0.5 air + 0.5 SF_6)	Density (kg m^{-3})			3.65		
	Specific heat ratio			1.16		
	Atwood number			0.50		
Inner cylinder (VF_1 air+ VF_2 SF_6)	VF_2	0.05	0.2	0.4	0.6	0.8
	Density (kg m^{-3})	1.45	2.19	3.17	4.14	5.11
	Specific heat ratio	1.35	1.25	1.18	1.14	1.12
	Atwood number	-0.43	-0.25	-0.07	0.06	0.17

III. RESULTS AND DISCUSSION

A. Evolution of the double-layer gas cylinder

In the numerical simulation of the double-layer gas cylinder evolution, the physical time (t) can be normalized by the velocity of the IS (W_i) and the diameter of the outer cylinder (D_0), represented by $\tau = tW_i/D_0$. Figure 3 displays the numerical schlieren images at various Atwood numbers. A comparison between these schlieren images for case I and experimental results³² reveals a close alignment in bubble morphologies and shock wave positions, which validates the accuracy of the numerical method.

Upon the impact of the IS on the upstream interface of the outer cylinder (UI_1), it transforms into the first transmitted shock wave (TS_1). The gas composition within the gas ring is consistent in various scenarios, resulting in a constant velocity for TS_1 ($\tau = 0.28$), which suggests that the moment when TS_1 impinges on the upstream interface of the inner cylinder (UI_2) keeps the same at different scenarios. Following the passage of TS_1 over UI_2 , it turns to the second transmitted shock wave (TS_2). As the concentrations of SF_6 in the inner cylinder increase, the acoustic impedance rises, thereby suppressing the propagation velocity of TS_2 in the inner cylinder ($\tau = 0.75$). The transition in morphology of TS_2 from divergence to convergence can also be observed, which induces diverse interface morphologies downstream of the outer cylinder (DI_1). When the Atwood numbers are below 0, the secondary vortex pair emerges at the DI_1 . The distance between the second vortex pairs decreases with increasing Atwood number. Due to the small distance between the vortex pair, they rapidly merge and form a jet at the later stage of evolution. When the Atwood numbers are above 0, a jet is formed at the DI_1 ($\tau > 2.45$). In the scenario of a single-layer gas cylinder, a downstream jet propagates from the downstream interface due to shock focusing.¹⁹ However, the wave patterns are complex due to the existence of an inner cylinder compared to the single-layer gas cylinder, further investigation is needed to understand the mechanisms behind the generation of secondary vortex pairs and downstream jets of the double-layer gas cylinder.

B. Formation of the secondary vortex pair and jet

Due to the sign of the Atwood number for the inner layer having an impact on the morphologies of the DI_1 , the mechanisms behind the formation of secondary vortex pairs and jets at DI_1 are discussed in this section to investigate the dependence of the flow morphologies on Atwood numbers.

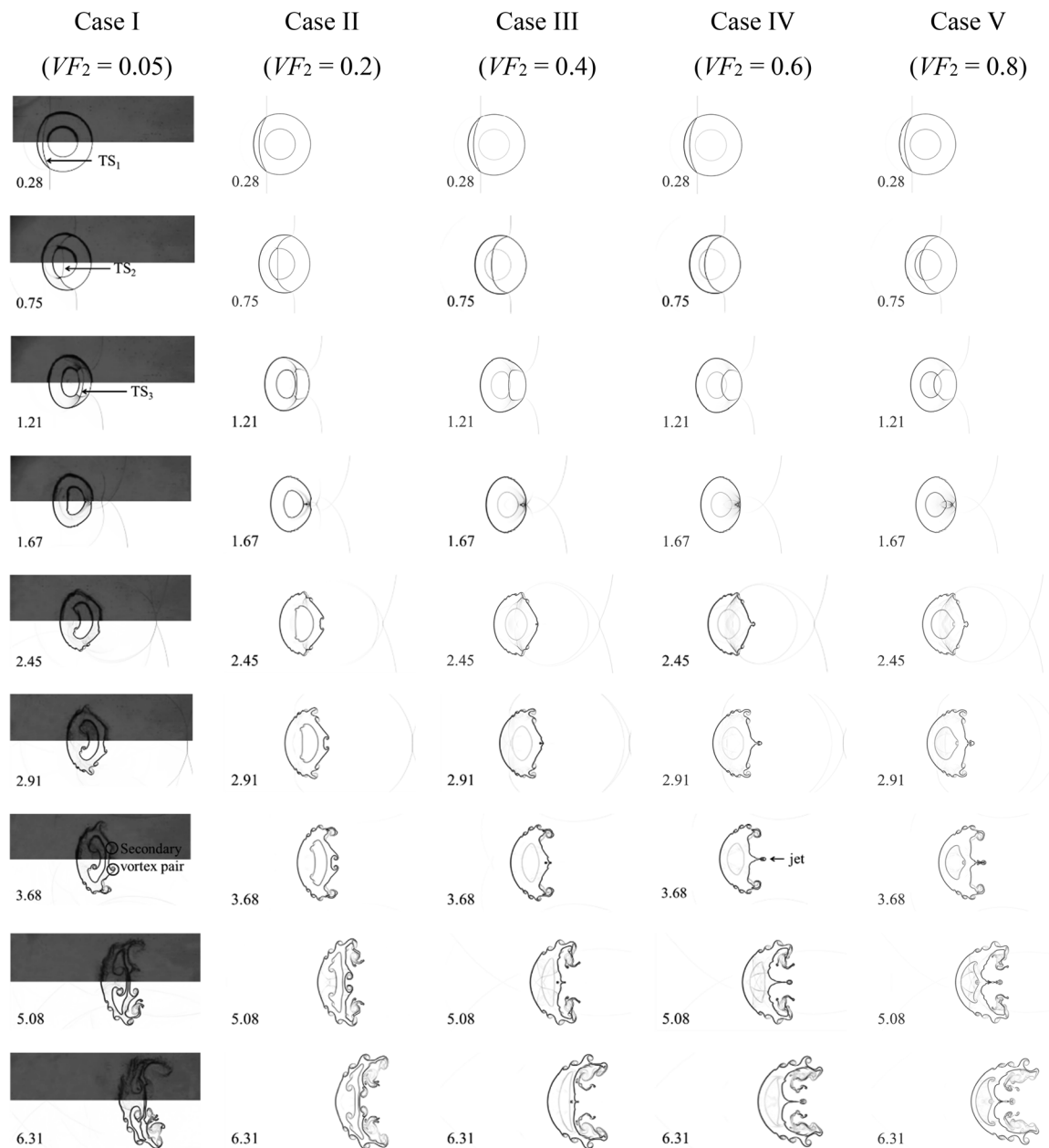


FIG. 3. Numerical schlieren images of the double-layer gas cylinders for different Atwood numbers.

For the scenarios of the Atwood numbers below 0 (see Figs. 4–6), the sweeping of a diffracted shock contributes to the formation of an internal diffracted transmitted shock wave (DTS) inside the bubble. Upon TS_2 passing over the downstream interface of the inner cylinder (DI_2), it turns into the third transmitted shock wave (TS_3). The shock k , the TS_3 , the DTS, and the reflected shock wave (RS) are connected by a Mach stem. As time progresses, these four shock waves intersect at one point. Subsequently, TS_3 separates from the other three shock waves, generating a new triple point (TP). It is noteworthy that the

position at which the triple points collide with the downstream interface coincides with the position of the vortex pair formation. Due to the interaction of shock waves, a high-pressure zone is formed downstream of the TP. As the triple points pass through DI_1 , the increase in pressure gradient and the change in density gradient lead to the generation of baroclinic vorticity, thereby inducing the formation of secondary vortex pairs.

As depicted in Figs. 4–6, the morphological transition of TS_2 shifts from divergence to convergence with increasing concentrations

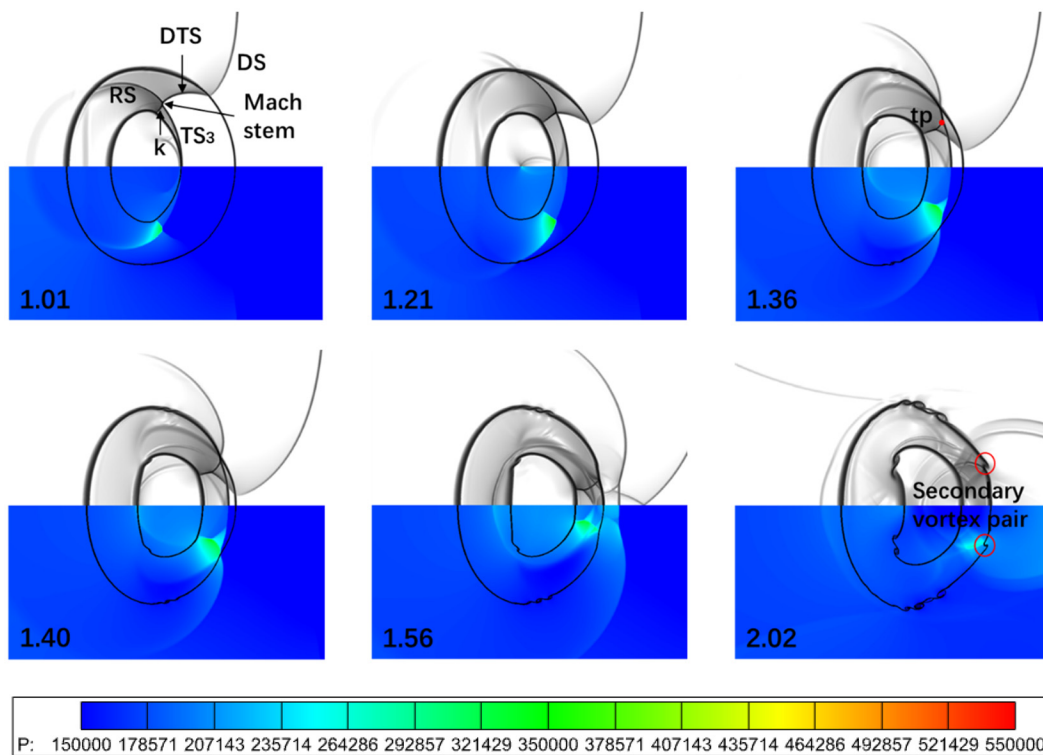


FIG. 4. Time sequences of numerical schlieren images and pressure contours for case I. DS, diffracted shock wave; DTS, diffracted transmitted shock wave; RS, reflected shock wave; TS_3 , the third transmitted shock wave; K, a shock wave; and TP, triple point.

of SF_6 in the inner cylinder. The morphology of TS_2 is divergent in case I, while the TS_2 tends to converge in case III. Therefore, when TS_2 passes through DI_2 , the distance between the Mach stem and the symmetry axis decreases, and the length of the Mach stem increases. With an increase in the Atwood number, the intersection point of the shock k , TS_3 , DTS, and RS moves closer to the symmetry axis. Following the separation of TS_3 from this point, the distance between the resulting triple points decreases. As the interaction between the triple points and DI_1 induces the formation of secondary vortex pairs, an increase in the Atwood number leads to a reduction in the distance between secondary vortex pairs.

Figures 7 and 8 reveal the scenarios of Atwood numbers over 0, where TS_2 exhibits a convergent morphology. The TS_3 , DTS, and RS meet at one point after TS_2 impinges on the DI_2 , and TS_3 does not separate from this point. The convergence of TS_3 , DTS, and its symmetric counterpart results in the formation of two high-pressure zones. After TS_3 passes through the intersection point of DTS and its symmetric counterpart, a significantly higher-pressure zone is generated downstream of TS_3 . As TS_3 continues to move and impinge on the downstream interface, it gives rise to the formation of a bulge, followed by the generation of a jet.

C. Widths and heights

The widths and heights of both outer and inner cylinders are investigated to quantitatively analyze the evolution process. For the outer cylinder, the compression effect of the IS on the UI_1 leads to a

reduction in widths at the early stage of evolution, as shown in Fig. 9(a). Since gas composition within the gas ring remains constant and the change in the gas composition of the inner cylinder has minimal impact on the morphologies of the outer interface before the passage of the IS, the widths and heights of various cases remain essentially unchanged ($\tau = 0-1.22$). As the Atwood number increases, the morphologies of the UI_2 transition from secondary vortex pairs to jets, leading to an increase in widths. As the concentration of SF_6 in the inner cylinder increases, the acoustic impedance increases, which slows down the propagation speed of the transmitted shock wave within the inner cylinder for the positive Atwood number cases. Consequently, the high-pressure zone associated with the TS_3 in case V reaches the DI_1 later than that in case IV, and the formation of the bulge and the jet is delayed (see Figs. 7 and 8), leading to a smaller width in case V compared to case IV. As depicted in Fig. 9(b), the heights of the outer cylinder remain unchanged during the early phase of the evolution ($\tau = 0-0.7$). After the IS passes through the highest point of the outer cylinder, a diffracted shock wave (DS) is generated, resulting in compression of the heights ($\tau = 0-1.22$). A large amount of baroclinic vorticity is deposited near the highest point of the outer interface, generating the primary vortex pair, which promotes the increase in heights. As the Atwood number increases, the morphologies of the inner cylinder noticeably transition from divergence to convergence, leading to a reduction in the growth rate of heights.

Figure 10 reveals the variation of the widths and heights of the inner cylinder. The physical time (t) can be normalized by $\tau' = tW'_i/d_0$,

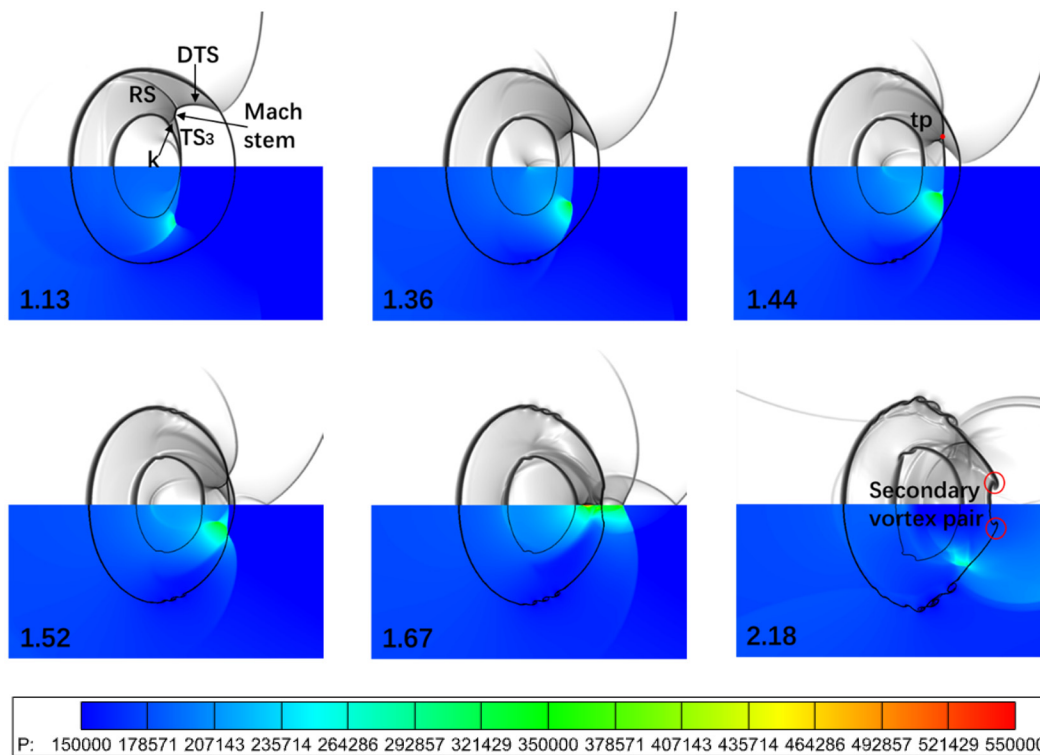


FIG. 5. Time sequences of numerical schlieren images and pressure contours for case II.

where W_1' represents the velocity of the first transmitted shock wave (TS_1) and d_0 represents the diameter of the inner cylinder. During the initial phase ($\tau' = 0-0.87$), the widths of the inner cylinder undergo a rapid decline due to the impact of the TS_1 with the Atwood number decreasing.

For the inner cylinder, the width in case V is significantly larger than that of other cases, and the heights will decrease due to their convergent pattern with the Atwood number increasing. During the initial phase ($\tau' = 0-0.87$), the widths of the inner cylinder undergo a rapid decline due to the influence of the TS_1 with the IS intensity increasing, as depicted in Fig. 5(a). This phenomenon occurs as the increased intensity of the TS_1 caused by the intense IS leads to compression on the UI_2 . Simultaneously, the intense IS compresses the outer interface, prompting an accelerated downstream displacement and subsequently causing compression on UI_2 , which results in a reduction in widths. Following this compression phase, the development of the DI_2 and the growth of the vortex pair contribute to an increase in the widths of the inner cylinder until it ultimately couples with the outer interface.

The compression of the inner cylinder in the flow direction by the shock wave promotes its spanwise development, contributing to a slight increase in heights at the early stage of the evolution ($\tau' = 0.4-0.75$). The heights are compressed due to the TS_1 passing over the highest points of the inner cylinder ($\tau' = 0.75-1.3$). As the intensity of IS increases, the development of the vortex pair in the spanwise direction is further enhanced, resulting in the growth of the heights, as illustrated in Fig. 5(b). However, at the later stage of evolution, an increase in the intensity of the IS accelerates the coupling between the vortex

pairs of the inner cylinders and the primary vortex pairs of the outer cylinders.

D. Vorticity generation

1. Dynamics of vorticity production

During the interaction between the shock waves and the gas cylinder, a large amount of vorticity is deposited at the interfaces, resulting in mixing. To investigate the mechanism of vorticity evolution, we introduce the vorticity transport equation by taking the curl of the momentum equation for compressible fluid, which is given as follows:⁴³

$$\frac{\partial \omega}{\partial t} = (\omega \cdot \nabla) u - \omega(\nabla \cdot u) + \frac{1}{\rho^2} (\nabla \rho \times \nabla p) + \frac{\mu}{\rho} \nabla^2 \omega, \quad (11)$$

where ω denotes the vorticity of each grid over the whole computational domain.

The first term on the right-hand of Eq. (11), referring to the stretching term, is crucial for 3D turbulence but is absent in this 2D model. The second term is the dilatation term, which holds significance solely in scenarios involving highly compressible fluids. The third term is the baroclinic term, which signifies the misalignment between pressure and density gradients, inducing the formation of small-scale rolled-up vortices at the bubble interface. The last term is the viscous term, denoting the rate at which vorticity changes due to molecular diffusion of vorticity. At the initial stage of evolution, the

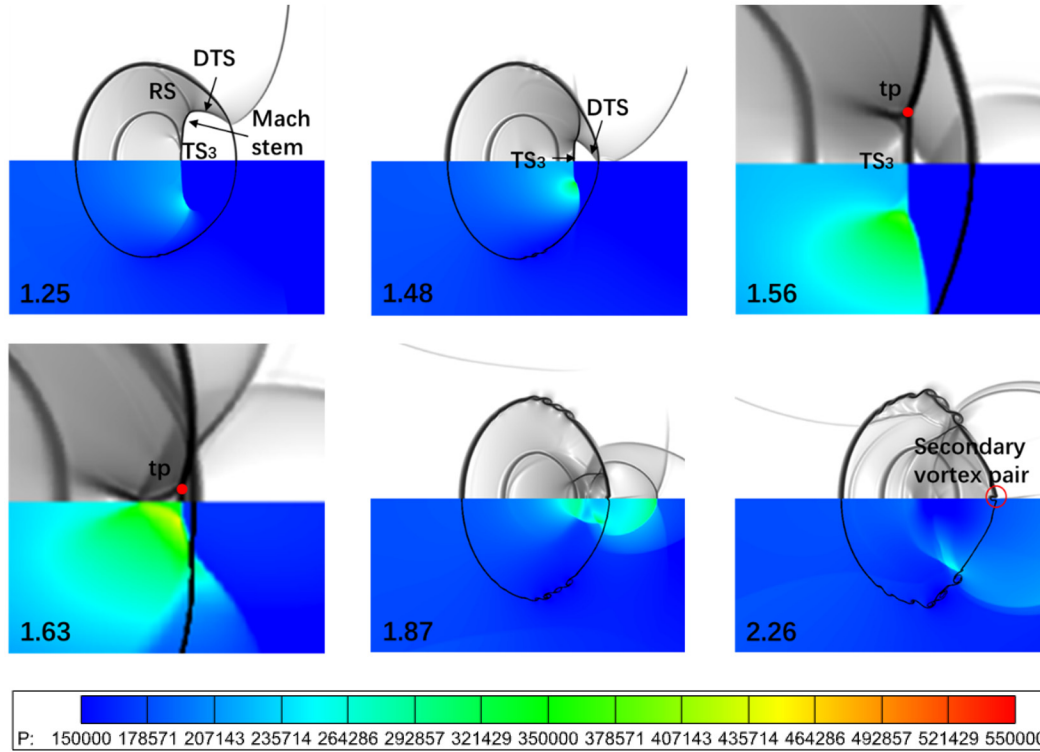


FIG. 6. Time sequences of numerical schlieren images and pressure contours for case III.

deposition of baroclinic vorticity on the bubble interface is widely considered to be the primary factor of vorticity production.

Figure 11 illustrates the impacts of the Atwood number on the vorticity distribution at various time sequences. Initially, the vorticity is uniformly 0. Following the passage of IS over the interfaces, the baroclinic vorticity is mainly deposited at the interfaces. Due to the nearly orthogonal nature of pressure and density gradients at the top and bottom regions of the gas cylinder, a large amount of vorticity is deposited in these regions. The vorticity along the axis of the gas cylinder is 0 due to the pressure and density gradients being collinear. The negative vorticity is generated at the outer interface of the double-layer gas cylinder. In the scenarios with negative Atwood numbers, positive vorticity is deposited at the inner interface, while in the scenarios with positive Atwood numbers, negative vorticity is deposited at the inner interface. As the IS propagates from the left boundary to the right boundary, the density gradient points inward radially for the light/heavy interface where the Atwood numbers are over 0, while it points outward for the heavy/light interface where the Atwood numbers are below 0, and the pressure gradient acts perpendicular to the upstream direction of the IS. With the growth of the Atwood number, the morphologies of the DI₁ transition from the secondary vortex pair to the downstream jet.

To have a further understanding for effects of the Atwood number on the vorticity production, the spatially integrated dilatation, baroclinic, and viscous terms are investigated in detail, which are given by

$$P_{\omega, \text{dil}} = - \frac{\int_D |\omega(\nabla \cdot \mathbf{u})| dxdy}{\int_D dxdy} = - \frac{\int_D \left| \omega \left(\frac{\partial u}{\partial x} + \frac{\partial v}{\partial y} \right) \right| dxdy}{\int_D dxdy}, \quad (12)$$

$$P_{\omega, \text{bar}} = \frac{\int_D \left| \frac{1}{\rho^2} (\nabla \rho \times \nabla p) \right| dxdy}{\int_D dxdy} = \frac{\int_D \left| \frac{1}{\rho^2} \left(\frac{\partial \rho}{\partial x} \frac{\partial p}{\partial y} - \frac{\partial \rho}{\partial y} \frac{\partial p}{\partial x} \right) \right| dxdy}{\int_D dxdy}, \quad (13)$$

$$P_{\omega, \text{vis}} = \frac{\int_D \left| \frac{\mu}{\rho} \nabla^2 \omega \right| dxdy}{\int_D dxdy} = \frac{\int_D \left| \frac{\mu}{\rho} \left(\frac{\partial^2 \omega}{\partial x^2} + \frac{\partial^2 \omega}{\partial y^2} \right) \right| dxdy}{\int_D dxdy}. \quad (14)$$

As illustrated in Fig. 12, the absolute values of the dilatational and baroclinic terms surpass that of the viscous term, indicating their dominance in vorticity production during the evolution. Following the passage of the IS over the UI₁ ($0.43 < \tau < 1.1$), the value of case I in the dilatation term is greater than other cases, implying that the large absolute values of the Atwood numbers result in stronger compression effects, especially for the compression stage of the IS acting on the UI₁. Moreover, the absolute values of the Atwood numbers increase, contributing to the growth of the density gradient, which leads to an increase in the baroclinic term due to the misalignment of the density

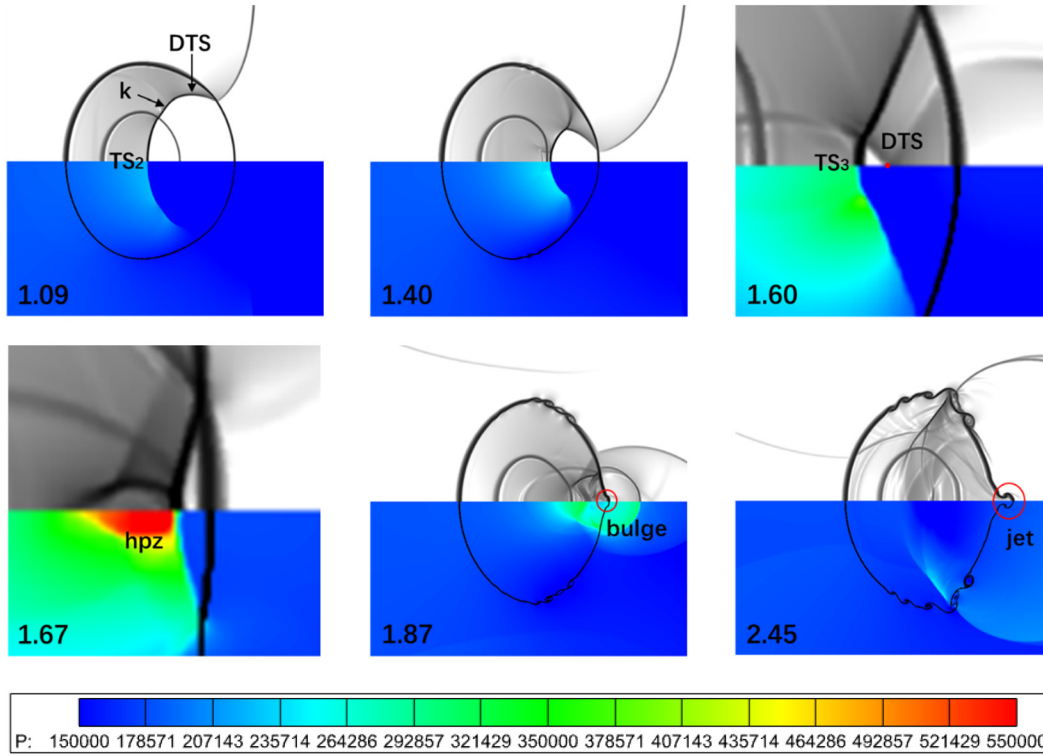


FIG. 7. Time sequences of numerical schlieren images and pressure contours for case IV. hpz, high-pressure zone.

and pressure gradients. For the scenarios of negative Atwood numbers, the first peak values occur after the TP impinges on the DI₁. The generation of the secondary vortex pairs and the presence of the stretched structures around the vortex core result in relatively large peak values of cases I and II in dilatation term. For the scenarios of positive Atwood numbers, the first peak values occur after the TS₃ with a much higher-pressure zone passing over the DI₁. The peak values of cases IV and V are relatively high due to an increase in density gradient. As time progresses, the values in baroclinic term remain elevated under the impact of the reflected shock structures.

2. Circulation

Integrating the vorticity over the computational domain gives the circulation

$$\Gamma = \iint_D \omega dx dy, \quad (15)$$

where D represents the area of the computational domain.

Figure 13 illustrates the positive, negative, and net components of the circulation, respectively. It can be observed that the magnitude of the positive circulation is consistently smaller than that of the negative circulation, resulting in a net circulation magnitude that remains below 0. The magnitude of the net circulation increases with the Atwood number rising.

It is evident that both positive and negative components of the circulation exhibit a linear change during the early stage of the

evolution. The net circulation can be predicted by linear summation of the positive circulation and negative circulation.³¹ Three circulation models are introduced to predict the net circulation of the double-layer gas cylinder. Notably, Picone and Boris (PB) model⁸ demonstrates effective prediction for the circulation of both shock-heavy gas cylinder and shock-light gas cylinder interactions. Samtaney and Zabusky (SZ) model⁴⁴ is suitable for predicting circulation in heavy gas cylinders. Yang, Kubota, and Zukoski (YKZ) model⁴⁵ is applicable for predicting circulation in light gas cylinders. The expressions of various circulation models are as follows:

$$\Gamma_{PB} = 2RV' \left(1 - \frac{V'}{2W_i} \right) \ln \left(\frac{\rho_0}{\rho_1} \right), \quad (16)$$

$$\Gamma_{SZ} = \begin{cases} \frac{4}{1+\gamma} \Gamma^*, & 0 < A < 0.2, \\ \frac{\pi+2}{1+\gamma} \Gamma^*, & A \geq 0.2, \end{cases} \quad (17)$$

$$\Gamma^* = \left(1 - \sqrt{\frac{\rho_0}{\rho_1}} \right) (1 + M^{-1} + 2M^{-2})(M-1)Rc_0, \quad (18)$$

$$\Gamma_{YKZ} = \frac{4R}{W_i} \frac{p'_0 - p_0}{\rho'_0} \frac{\rho_1 - \rho_0}{\rho_1 + \rho_0},$$

where V' represents the flow velocity behind the shock, ρ_0 and ρ'_0 are the pre-shocked and post-shocked density of the ambient air, while ρ_1 is the pre-shocked density of the gas within the gas ring. Similarly, p_0

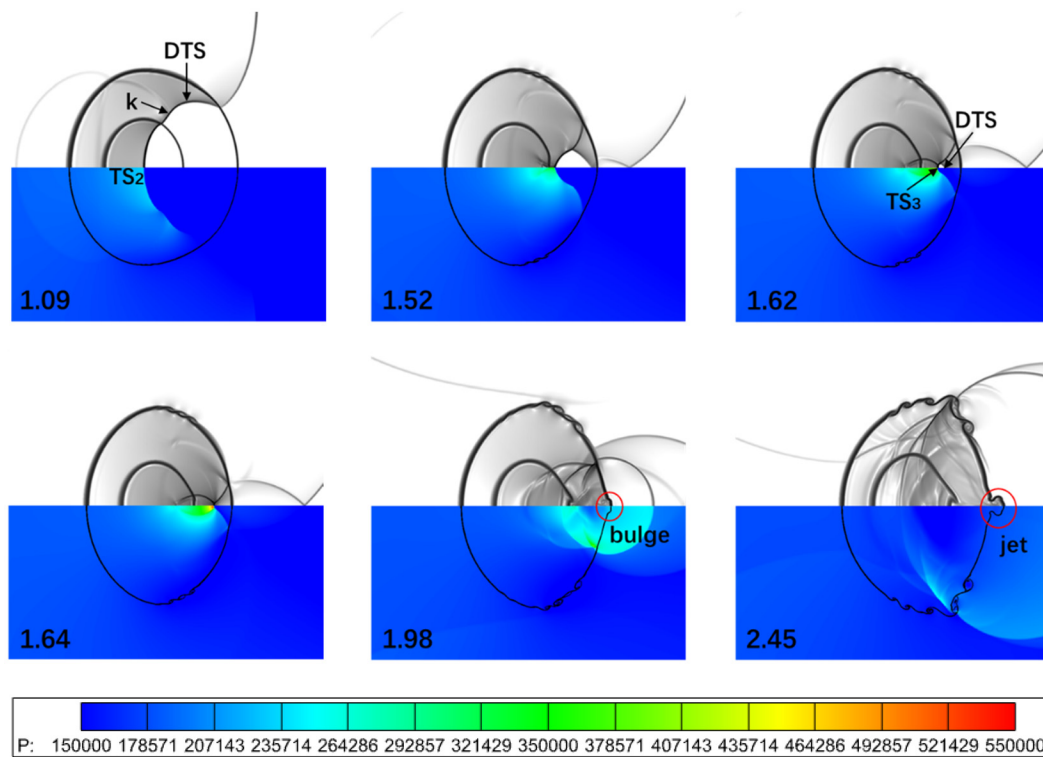


FIG. 8. Time sequences of numerical schlieren images and pressure contours for case V. TS_2 , the second transmitted shock wave.

and p'_0 are the pre-shocked and post-shocked pressure of the ambient air. $\gamma = (\gamma_0 + \gamma_1)/2$, γ_0 , and γ_1 denote the specific heat ratio of the ambient air and the gas within the gas ring. c_0 represents the sound speed of the ambient air.

Since the Atwood numbers for the outer cylinders are greater than 0, the process of IS passing through the outer cylinder can be viewed as the shock-heavy gas cylinder interaction, the circulation of

which can be predicted using either the PB model or the SZ model. For the scenarios where the Atwood numbers are below 0 for the inner cylinder, the passage of TS_1 over the inner cylinder can be regarded as the shock-light gas cylinder interaction, the circulation of which can be predicted by the PB model or YKZ model. After linearly summing the PB model or SZ model for the outer cylinder and the PB model or YKZ model for the inner cylinder, the comparison of net circulation

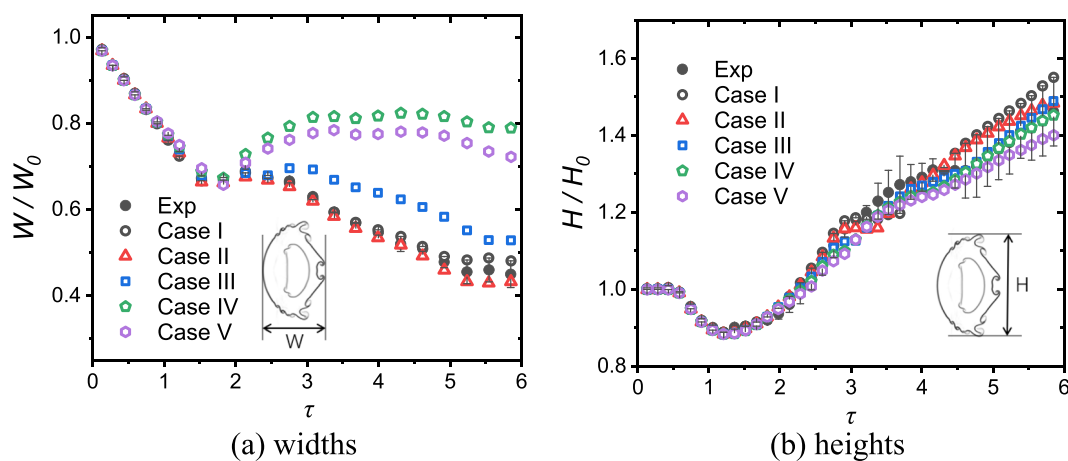


FIG. 9. Variation of the widths (a) and heights (b) of the outer cylinder.

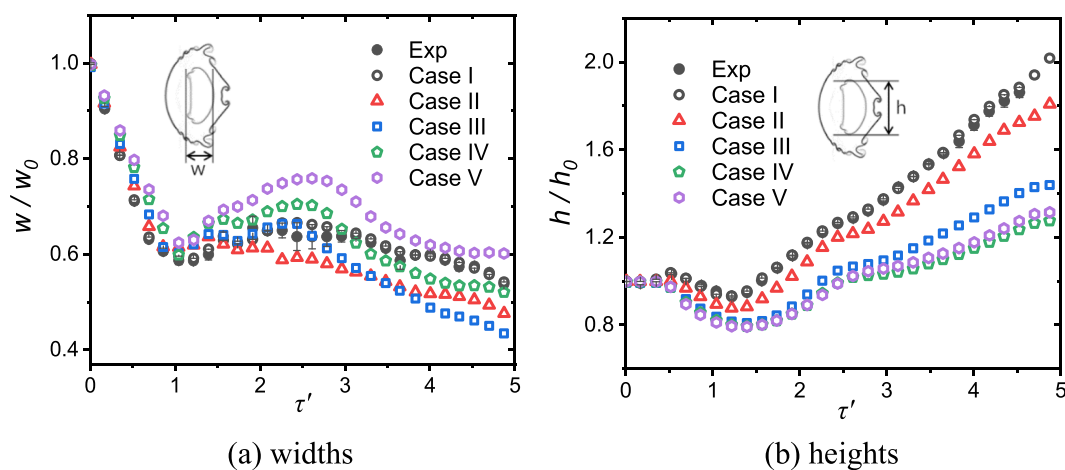


FIG. 10. Variation of the widths (a) and heights (b) of the inner cylinder.

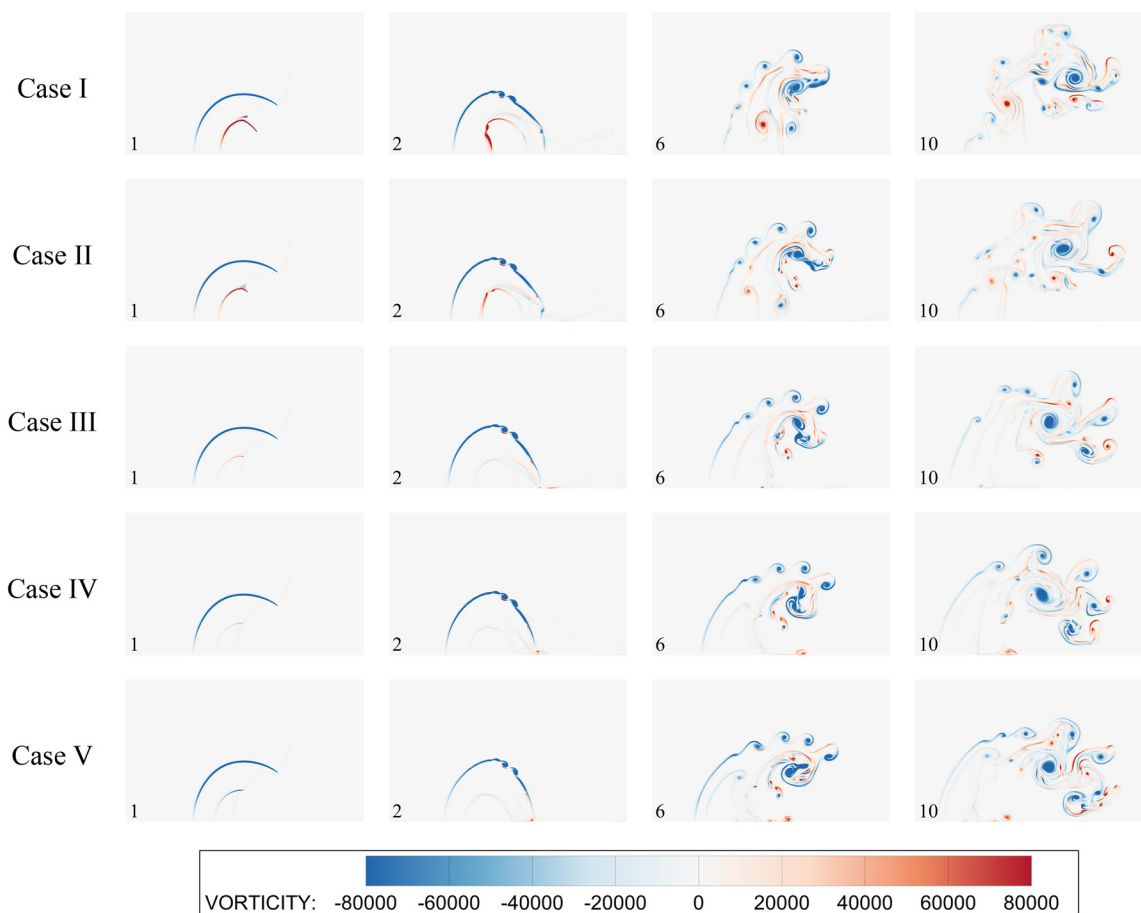


FIG. 11. Time sequences of vorticity distribution for different cases.

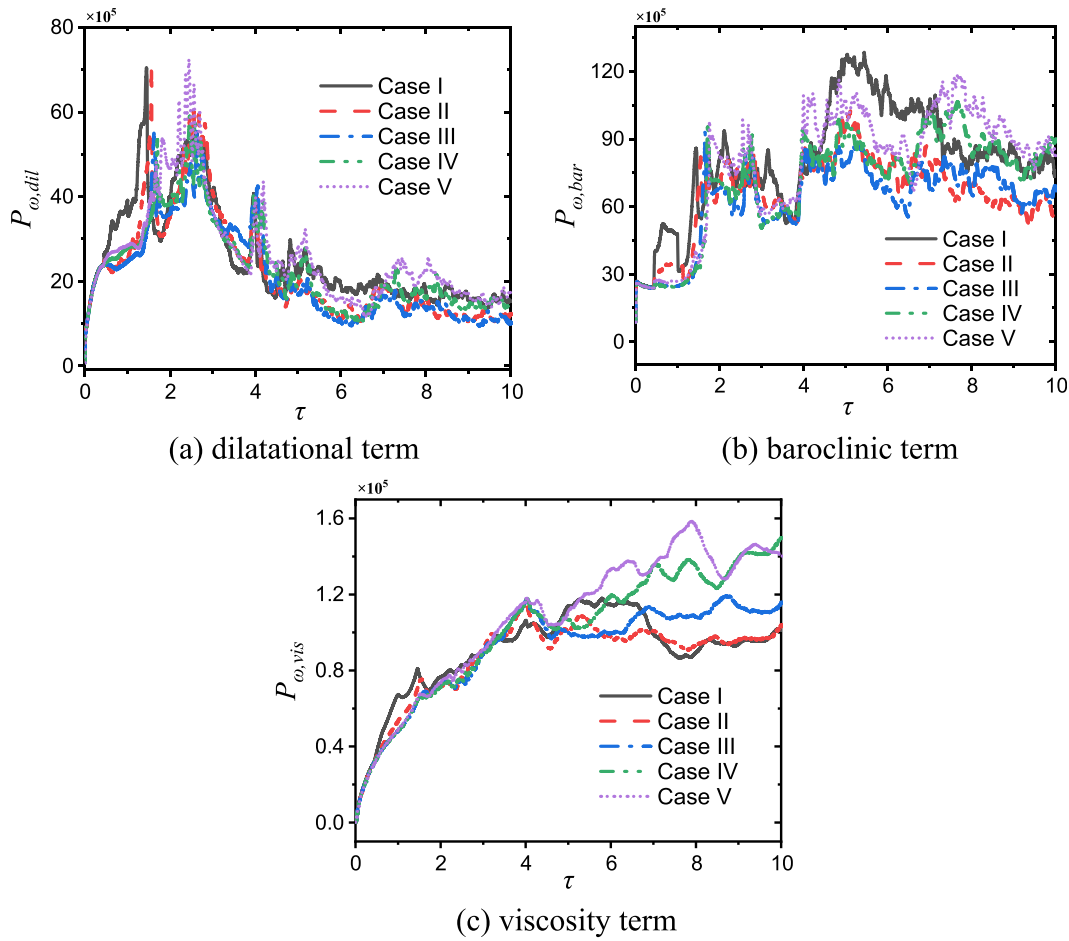


FIG. 12. Spatially integrated fields of the dilatation term (a), baroclinic term (b), and viscosity term (c).

between numerical and theoretical results is presented in Table V. The findings reveal that the absolute value of the relative error obtained from the summation of the SZ model and PB model is under 5%, indicating an accurate prediction of net circulation.

For scenarios where the Atwood numbers are above 0 for the inner cylinder, the passage of TS_1 over the inner cylinder can be considered as the shock-heavy gas cylinder interaction. Similarly, the circulation in these cases can be predicted using either the PB or SZ model. After linear summation of the PB model or SZ model for the outer cylinder and the PB model or SZ model for the inner cylinder, the comparison of net circulation between numerical and theoretical results is listed in Table VI. The results indicate that the summation of SZ and PB models or SZ and SZ models accurately predict the net circulation, with the absolute value of the relative error being under 5%.

E. Mixing

To explore the impacts of the Atwood number on the mixing of different gases, the area histories and mean mass fraction histories of the outer cylinder and inner cylinder are analyzed. Overall statistics for the double-layer gas cylinder cannot accurately reflect the individual

evolution of the gas ring and inner cylinder. Therefore, SF_6 in the inner cylinder is replaced by a hypothetical gas with the same physical properties. By tracking the mass fractions of SF_6 and the hypothetical gas in the gas ring and the inner cylinder, the physical quantities of the gas ring and the inner cylinder can be distinguished. Among which, S_{outer}^0 represents the area of the gas ring, while S_{outer} represents the area where the mass fraction of SF_6 within the gas ring is greater than 0.01. Similarly, S_{inner}^0 denotes the area of the inner cylinder, while S_{inner} denotes the area where the mass fraction of SF_6 within the inner cylinder is greater than 0.01. The equation of the mean mass fraction is given as follows:

$$\bar{C} = \frac{\iint_C C dx dy}{\iint_B dx dy}, \quad (19)$$

where C is the mass fraction of SF_6 at each grid within the gas cylinder, and B denotes the bubble. For the double-layer gas cylinder, \bar{C}_{outer}^0 represents the mean mass fraction of SF_6 of the gas ring at the initial condition, while \bar{C}_{outer} represents the mean mass fraction of SF_6 of the gas

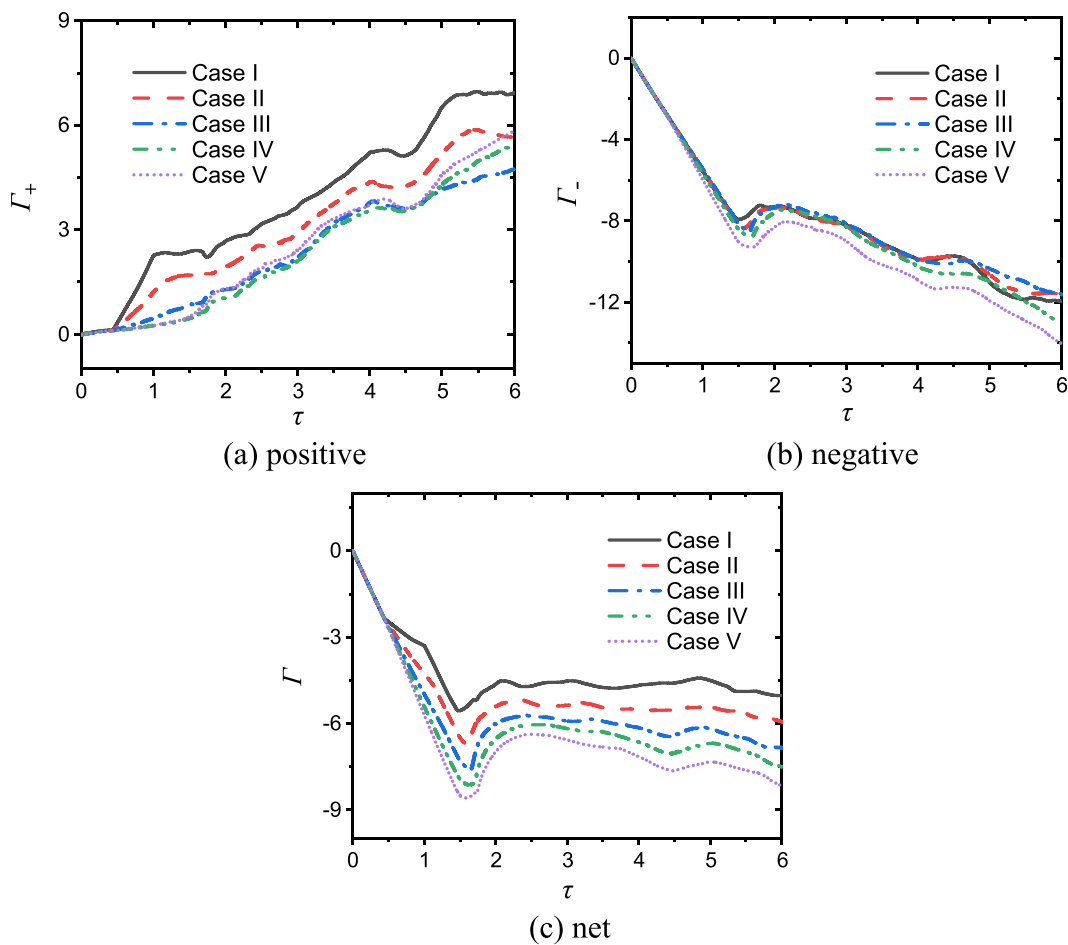


FIG. 13. The positive (a), negative (b), and net (c) components of the circulation.

TABLE V. Comparison of circulation from the numerical simulation results (Γ_{sim}) and theoretical predictions by the summation of different models when the Atwood numbers are below 0 for the inner cylinder (the unit of circulation is m^2/s).

Cases	Γ_{sim}	$\Gamma_{\text{PB+PB}}$	Error	$\Gamma_{\text{PB+YKZ}}$	Error	$\Gamma_{\text{SZ+PB}}$	Error	$\Gamma_{\text{SZ+YKZ}}$	Error
Case I	−5.56	−5.07	8.81%	−5.76	3.60%	−5.39	3.06%	−6.09	9.53%
Case II	−6.65	−6.02	9.47%	−6.37	4.21%	−6.35	4.51%	−6.70	0.75%
Case III	−7.51	−6.88	8.39%	−6.98	7.06%	−7.21	3.99%	−7.30	2.80%

TABLE VI. Comparison of circulation from the numerical simulation results (Γ_{sim}) and theoretical predictions by the summation of different models when the Atwood numbers are below 0 for the inner cylinder (the unit of circulation is m^2/s).

Cases	Γ_{sim}	$\Gamma_{\text{PB+PB}}$	Error	$\Gamma_{\text{PB+SZ}}$	Error	$\Gamma_{\text{SZ+PB}}$	Error	$\Gamma_{\text{SZ+SZ}}$	Error
Case IV	−8.02	−7.51	6.36%	−7.57	5.61%	−7.83	2.37%	−7.89	1.62%
Case V	−8.31	−8.00	3.73%	−8.12	2.29%	−8.32	0.12%	−8.44	1.54%

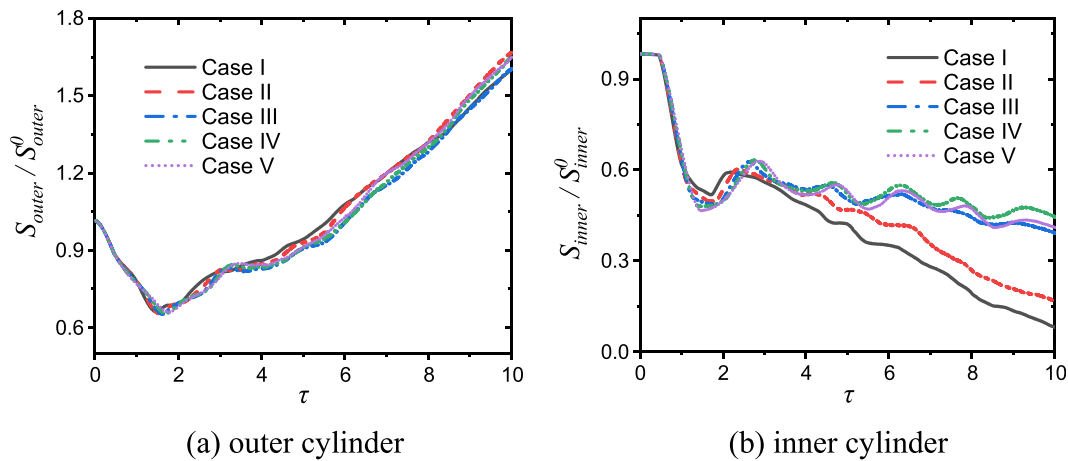


FIG. 14. Area histories of the outer cylinder (a) and inner cylinder (b).

ring. Similarly, \bar{C}_{inner}^0 denotes the mean mass fraction of SF_6 of the inner cylinder at the initial condition, while \bar{C}_{inner} denotes the mean mass fraction of SF_6 of the inner cylinder.

As depicted in Fig. 14, the gas cylinder undergoes compression initially due to the impact of IS at the early stage, leading to a reduction in area. For the outer cylinder, a secondary vortex pair and jet are formed and continue to develop following the shock passage over the outer interface, causing an increase in area. Due to the constant Atwood numbers of the outer cylinder, variations in the Atwood number of the inner cylinder have minimal influence on changes in the outer interfacial area. For the inner gas cylinder, as the Atwood number decreases, the vortex pairs develop upstream and couple with the outer interface, resulting in a reduction in the area of the inner cylinder at the later stage of the evolution.

Figure 15 illustrates the mean mass fraction of both outer and inner cylinders. As the Atwood number decreases, the concentration of SF_6 in the outer gas cylinder increases following the passage of the IS over the outer interface, which mainly results from the less ambient gas diffusing into the outer cylinder. Meanwhile, the concentration of

SF_6 in the inner gas cylinder significantly decreases, indicating more ambient gas diluting the SF_6 and promoting the mixing of different gases.

IV. CONCLUSIONS

The A/B/C-type gas cylinder with different concentrations of SF_6 (ranging from 5% to 80% in volume fraction) in the inner cylinder is constructed to investigate the dependence of the interface evolution on the Atwood number. Numerical simulations are conducted using a multi-block parallel finite-volume CFD code.

Flow patterns converge as the Atwood numbers exceed 0, while they diverge for negative Atwood numbers. This characteristic can be confirmed through numerical schlieren images. In scenarios with negative Atwood numbers, secondary vortex pairs emerge at the downstream interface of the outer cylinder, with the distance between them decreasing as the Atwood number is increased. However, a jet is generated at the downstream interface for positive Atwood numbers, supplanting the formation of secondary vortex pairs. Upon the analysis of pressure contours over various time sequences, it becomes evident that

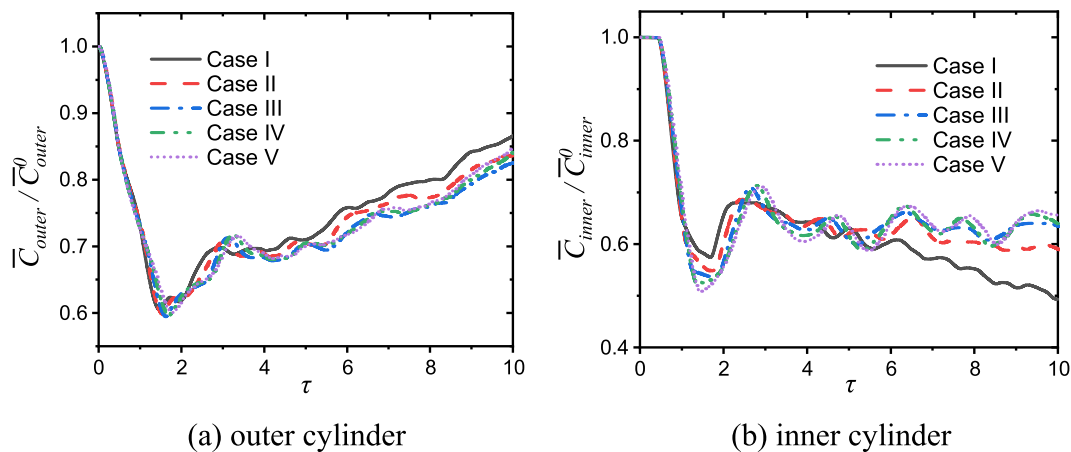


FIG. 15. Mean mass fraction histories of the outer cylinder (a) and inner cylinder (b).

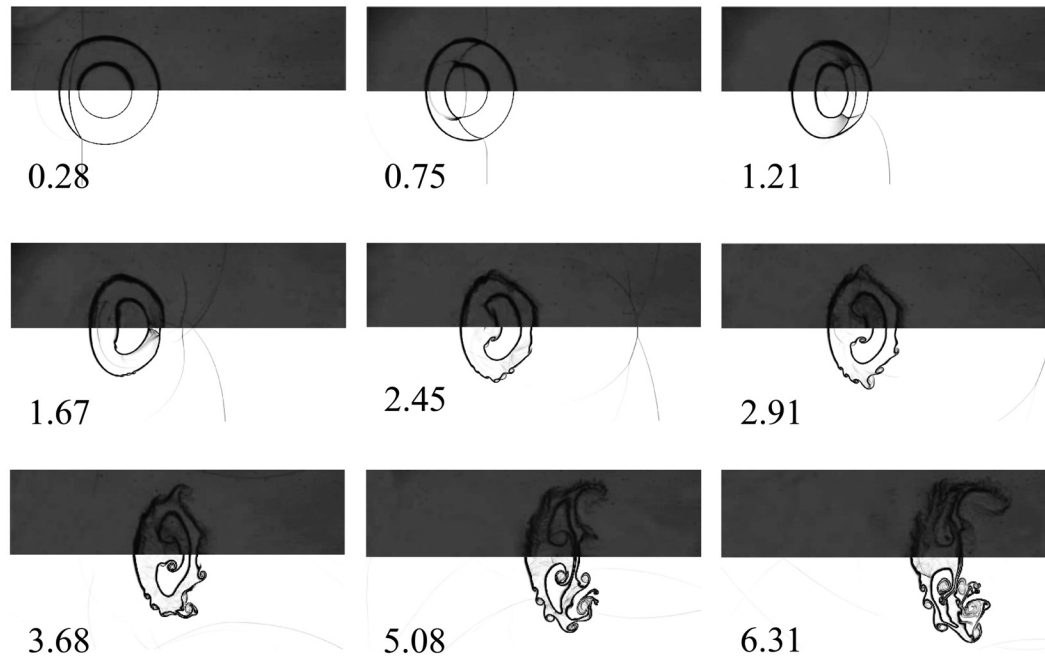


FIG. 16. Comparison of numerical schlieren images at different time sequences with the experimental results from Ref. 32.

a large amount of baroclinic vorticity is deposited at the interface following the interaction of a high-pressure triple point with the downstream interface in the cases of negative Atwood numbers. Conversely, a notably higher-pressure zone is generated after the transmitted shock wave traverses the convergence point due to the convergence of the shock waves. As the transmitted shock wave propagates and collides with the downstream interface, a bulge forms, subsequently giving rise to a jet. To quantify the process of the interface evolution, the changes in widths and heights of the outer and inner gas cylinders are analyzed with the Atwood number increasing. For the outer cylinder, the widths expand owing to the formation of a downstream jet, while the heights contract due to the convergence of the inner cylinder. For the inner cylinder, the heights decrease due to their convergent pattern. The vorticity transport equation is introduced to investigate the mechanism of vorticity evolution. The dilatation and baroclinic terms play a dominant role in vorticity production. For the positive Atwood number scenarios, the generation of the secondary vortex pairs and the presence of the stretched structures around the vortex core contribute to higher values of the first peak of cases I and II in the dilatation term. For the negative Atwood number scenarios, the peak values of cases IV and V are relatively high due to an increase in density gradient. The approach to predict the net circulation is linearly summing the circulation models. The findings reveal that the summation of the SZ and PB model can predict the circulation of positive Atwood number cases, while the summation of the SZ and PB model or SZ and SZ model can predict the circulation of negative Atwood number cases. The area and mean mass fraction histories of the outer and inner cylinders are analyzed to explore the gas mixing. As the Atwood number decreases, more ambient gas dilutes the SF_6 and promotes the gas mixing.

Expanding on the research in ICF and scramjet engines, it is observed that a reduction in the Atwood number can enhance the mixing of different materials, thereby decreasing the concentration of the inner

fuel, which may result in ignition failure. Furthermore, when the Atwood number is greater than 0, shock-focusing phenomena occur near the upstream of the DI, accompanied by the formation of a high-temperature and high-pressure zone, potentially leading to ignition of the inner fuel. Therefore, in the design of ICF capsules and scramjet engines, it is critical to ensure that the Atwood number of the inner gas cylinder remains positive. The corresponding experiments are suggested to consider different Atwood number combinations of the double-layer gas cylinder.

ACKNOWLEDGMENTS

We acknowledge the support of the Hong Kong Research Grants Council (No. 15207420).

AUTHOR DECLARATIONS

Conflict of Interest

The authors have no conflicts to disclose.

Author Contributions

Xin Li: Conceptualization (lead); Data curation (equal); Formal analysis (lead); Investigation (lead); Methodology (lead); Writing – original draft (lead); Writing – review & editing (equal). **Jiaao Hao:** Data curation (equal); Funding acquisition (lead); Supervision (lead); Writing – review & editing (lead). **Chih-Yung Wen:** Funding acquisition (equal); Supervision (equal). **E. Fan:** Data curation (equal).

DATA AVAILABILITY

The data that support the findings of this study are available from the corresponding author upon reasonable request.

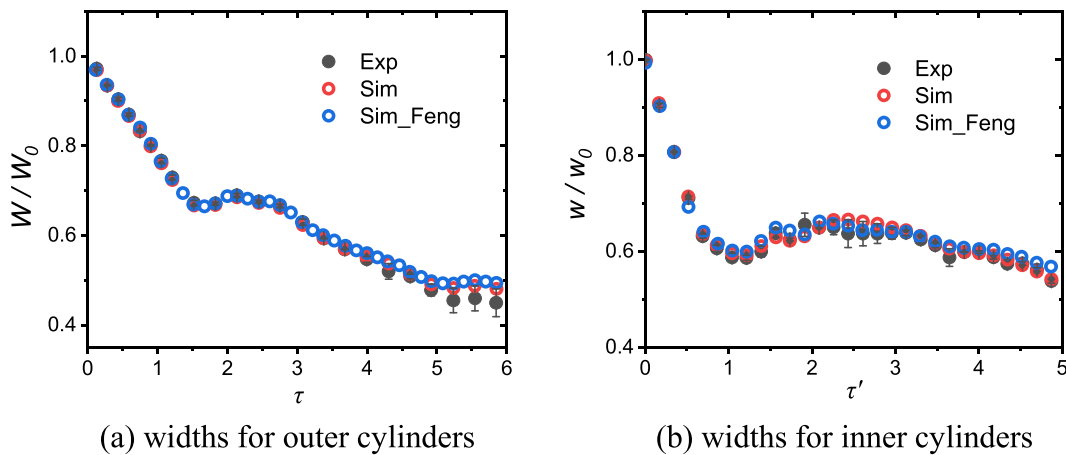


FIG. 17. Comparison of the calculated widths for (a) outer cylinders and (b) inner cylinders (the red circle) with the experimental (the black circle) and numerical results (the blue circle) from Ref. 32.

APPENDIX: NUMERICAL METHOD VALIDATION

Figure 16 provides a comparison between numerical schlieren images for case I and experimental results.³² The results reveal that the morphologies of the gas cylinder and the position of shock waves agree with the experimental data. In addition, Fig. 17 illustrates the comparison of the calculated widths for both the outer and inner cylinders, marking the error bars between the numerical and experimental results. It can be observed that the calculated widths are in good alignment with the experimental results. Through qualitative and quantitative comparisons, this numerical method is suitable for simulating the interaction between the IS and the double-layer gas cylinder.

REFERENCES

- R. D. Richtmyer, "Taylor instability in shock acceleration of compressible fluids," *Commun. Pure Appl. Math.* **13**(2), 297–319 (1960).
- E. E. Meshkov, "Instability of the interface of two gases accelerated by a shock wave," *Fluid Dyn.* **4**(5), 101–104 (1972).
- J. Lindl *et al.*, "Review of the National Ignition Campaign 2009–2012," *Phys. Plasmas* **21**(2), 020501 (2014).
- J. Shimoda, T. Inoue, Y. Ohira, R. Yamazaki, A. Bamba, and J. Vink, "On cosmic-ray production efficiency at supernova remnant shocks propagating into realistic diffuse interstellar medium," *Astrophys. J.* **803**(2), 98 (2015).
- J. Yang, T. Kubota, and E. E. Zukoski, "Applications of shock-induced mixing to supersonic combustion," *AIAA J.* **31**(5), 854–862 (1993).
- J. F. Haas, "Interaction of weak shock waves with cylindrical and spherical gas inhomogeneities," *J. Fluid Mech.* **181**, 41–76 (1987).
- K. H. A. Winkler, J. W. Chalmers, S. W. Hodson, P. R. Woodward, and N. J. Zabusky, "A numerical laboratory," *Phys. Today* **40**(10), 28–37 (1987).
- J. M. Picone and J. P. Boris, "Vorticity generation by shock propagation through bubbles in a gas," *J. Fluid Mech.* **189**, 23–51 (1988).
- J. W. Jacobs, "The dynamics of shock accelerated light and heavy gas cylinders," *Phys. Fluids A* **5**(9), 2239–2247 (1993).
- C. Tomkins, S. Kumar, G. Orlicz, and K. Prestridge, "An experimental investigation of mixing mechanisms in shock-accelerated flow," *J. Fluid Mech.* **611**, 131–150 (2008).
- X. Wang, D. Yang, J. Wu, and X. Luo, "Interaction of a weak shock wave with a discontinuous heavy-gas cylinder," *Phys. Fluids* **27**(6), 064104 (2015).
- J. Ding, T. Si, M. Chen, Z. Zhai, X. Lu, and X. Luo, "On the interaction of a planar shock with a three-dimensional light gas cylinder," *J. Fluid Mech.* **828**, 289–317 (2017).
- J. Ding, Y. Liang, M. Chen, Z. Zhai, T. Si, and X. Luo, "Interaction of planar shock wave with three-dimensional heavy cylindrical bubble," *Phys. Fluids* **30**(10), 106109 (2018).
- A. Bagabir and D. Drikakis, "Mach number effects on shock-bubble interaction," *Shock Waves* **11**, 209–218 (2001).
- J. H. J. Niederhaus, J. A. Greenough, J. G. Oakley, D. Ranjan, M. H. Anderson, and R. Bonazza, "A computational parameter study for the three-dimensional shock-bubble interaction," *J. Fluid Mech.* **594**, 85–124 (2008).
- Z. G. Zhai, T. Si, L. Y. Zou, and X. S. Luo, "Jet formation in shock-heavy gas bubble interaction," *Acta Mech. Sin./Lixue Xuebao* **29**(1), 24–35 (2013).
- Y. Zhu, L. Yu, J. Pan, Z. Pan, and P. Zhang, "Jet formation of SF₆ bubble induced by incident and reflected shock waves," *Phys. Fluids* **29**(12), 126105 (2017).
- B. Guan, H. Yang, H. Yang, and G. Wang, "On the irregular jet formation of shock-accelerated spherical heavy gas bubbles," *Phys. Fluids* **34**(12), 126111 (2022).
- J. Ou, J. Ding, X. Luo, and Z. Zhai, "Effects of Atwood number on shock focusing in shock-cylinder interaction," *Exp. Fluids* **59**(2), 29 (2018).
- J. D. Lindl *et al.*, "The physics basis for ignition using indirect-drive targets on the National Ignition Facility," *Phys. Plasmas* **11**(2), 339–491 (2004).
- K. O. Mikaelian, "Richtmyer-Meshkov instabilities in stratified fluids," *Phys. Rev. A* **31**(1), 410–419 (1985).
- K. O. Mikaelian, "Rayleigh-Taylor and Richtmyer-Meshkov instabilities in multilayer fluids with surface tension," *Phys. Rev. A* **42**(12), 7211–7225 (1990).
- K. O. Mikaelian, "Rayleigh-Taylor and Richtmyer-Meshkov instabilities in finite-thickness fluid layers," *Phys. Fluids* **7**(4), 888–890 (1995).
- K. O. Mikaelian, "Numerical simulations of Richtmyer-Meshkov instabilities in finite-thickness fluid layers," *Phys. Fluids* **8**(5), 1269–1292 (1996).
- M. T. Henry de Frahan, P. Movahed, and E. Johnsen, "Numerical simulations of a shock interacting with successive interfaces using the Discontinuous Galerkin method: The multilayered Richtmyer-Meshkov and Rayleigh-Taylor instabilities," *Shock Waves* **25**(4), 329–345 (2015).
- W. Liu *et al.*, "Theoretical study on finite-thickness effect on harmonics in Richtmyer-Meshkov instability for arbitrary Atwood numbers," *Phys. Plasmas* **25**(12), 122103 (2018).
- Y. Liang, L. Liu, Z. Zhai, T. Si, and C. Y. Wen, "Evolution of shock-accelerated heavy gas layer," *J. Fluid Mech.* **886**, A7 (2020).
- Y. Liang and X. Luo, "On shock-induced heavy-fluid-layer evolution," *J. Fluid Mech.* **920**, A13 (2021).
- Y. Liang and X. Luo, "On shock-induced light-fluid-layer evolution," *J. Fluid Mech.* **933**, A10 (2022).
- Z. Cong, X. Guo, T. Si, and X. Luo, "Experimental and theoretical studies on heavy fluid layers with reshock," *Phys. Fluids* **34**(10), 104108 (2022).

- ³¹G. Wang, Y. Wang, D. Li, and B. Guan, "Numerical study on shock-accelerated gas rings," *Phys. Fluids* **32**(2), 026102 (2020).
- ³²L. Feng, J. Xu, Z. Zhai, and X. Luo, "Evolution of shock-accelerated double-layer gas cylinder," *Phys. Fluids* **33**(8), 086105 (2021).
- ³³L. Feng, Z. Zhai, T. Si, and X. Luo, "Eccentric effect on evolution of shock-accelerated double-layer gas cylinder," *Phys. Gases* **7**(2), 13–25 (2022) (in Chinese).
- ³⁴X. Li, J. Hao, C. Y. Wen, and E. Fan, "Effects of Mach and Atwood numbers on the shock-induced evolution of a double-layer gas cylinder," *Phys. Fluids* **36**(2), 022108 (2024).
- ³⁵D. S. Montgomery *et al.*, "Design considerations for indirectly driven double shell capsules," *Phys. Plasmas* **25**(9), 092706 (2018).
- ³⁶B. M. Haines *et al.*, "Constraining computational modeling of indirect drive double shell capsule implosions using experiments," *Phys. Plasmas* **28**(3), 032709 (2021).
- ³⁷Y. Liang and X. Luo, "On shock-induced evolution of a gas layer with two fast/slow interfaces," *J. Fluid Mech.* **939**, A16 (2022).
- ³⁸J. Hao and C. Y. Wen, "Numerical investigation of oxygen thermochemical nonequilibrium on high-enthalpy double-cone flows," *Int. J. Heat Mass Transfer* **127**, 892–902 (2018).
- ³⁹J. Hao, J. Wang, and C. Lee, "Numerical simulation of high-enthalpy double-cone flows," *AIAA J.* **55**(7), 2471–2475 (2017).
- ⁴⁰J. Hao, C. Y. Wen, and J. Wang, "Numerical investigation of hypervelocity shock-wave/boundary-layer interactions over a double-wedge configuration," *Int. J. Heat Mass Transfer* **138**, 277–292 (2019).
- ⁴¹E. F. Toro, M. Spruce, and W. Speares, "Restoration of the contact surface in the HLL-Riemann solver," *Shock Waves* **4**, 25–34 (1994).
- ⁴²B. Van Leer, "Towards the ultimate conservative difference scheme. II. Monotonicity and conservation combined in a second-order scheme," *J. Comput. Phys.* **14**, 361–370 (1974).
- ⁴³D. Ranjan, J. Oakley, and R. Bonazza, "Shock-bubble interactions," *Annu. Rev. Fluid Mech.* **43**, 117–140 (2011).
- ⁴⁴J. Yang, T. Kubota, and E. E. Zukoski, "A model for characterization of a vortex pair formed by shock passage over a light-gas inhomogeneity," *J. Fluid Mech.* **258**, 217–244 (1994).
- ⁴⁵N. J. Zabusky and S. M. Zeng, "Shock cavity implosion morphologies and vortical projectile generation in axisymmetric shock-spherical fast/slow bubble interactions," *J. Fluid Mech.* **362**, 327–346 (May 1998).